

Source-independent time-lapse full-waveform inversion for VTI media

Yanhua Liu & Ilya Tsvankin

*Center for Wave Phenomena and Dept. of Geophysics, Colorado School of Mines, Golden CO 80401
email liuyanhua@mines.edu*

ABSTRACT

Time-lapse full-waveform inversion (TLFWI) can provide high-resolution information about changes in the reservoir properties during hydrocarbon production and CO_2 injection. However, the accuracy of the estimated source wavelet, which is critically important for TLFWI, is often insufficient for field-data applications. The so-called “source-independent” FWI is designed to reduce the influence of the source wavelet on the inversion results. Here, we incorporate the convolution-based source-independent technique into a time-lapse FWI algorithm for VTI (transversely isotropic with a vertical symmetry axis) media. The gradient of the modified FWI objective function is obtained from the adjoint-state method. The algorithm is tested on a model with a graben structure and the modified VTI Marmousi model using three time-lapse strategies (the parallel-difference, sequential-difference, and double-difference methods). The results confirm the ability of the developed methodology to reconstruct the localized time-lapse parameter variations even for a strongly distorted source wavelet. The algorithm remains robust in the presence of moderate noise in the input data but the accuracy of the estimated time-lapse changes depends on the model complexity.

Key words: Time-lapse seismic, source-independent technique, full-waveform inversion, multicomponent data, elastic inversion, anisotropy, VTI media

1 INTRODUCTION

Because seismic signatures are sensitive to the changes (e.g., in pressure and saturation) inside the reservoir, seismic time-lapse monitoring has been widely used for optimizing hydrocarbon production and CO_2 injection (Lumley, 2010; Smith and Tsvankin, 2013; Pevzner et al., 2017). Full-waveform inversion (FWI) is an established tool for high-resolution velocity analysis and has been applied to reservoir characterization (Vigh et al., 2014; Asnaashari et al., 2015; Singh et al., 2018). FWI iteratively updates the medium parameters by minimizing the misfit between the observed and simulated seismic data.

Unlike conventional time-lapse methods, FWI operates with both the phase and amplitude of seismic waves, which can potentially increase the resolution of the inverted time-lapse parameter variations. However, FWI requires an accurate estimate of the source wavelet. Errors in the source signature (e.g., in its shape, frequency, or amplitude) can hinder matching of the simulated and observed data and distort the inversion results (Song et al., 1995; Pratt, 1999; Warner et al., 2013; Luo et al., 2014; Yuan et al., 2014). This issue is particularly important for time-lapse FWI because the source wavelet can be different (non-repeatable) for the baseline and monitor surveys.

One way to reconstruct the source wavelet in FWI is to iteratively estimate it during the inversion along with the medium parameters (Song et al., 1995; Pratt, 1999; Xu et al., 2006). However, this method incurs a substantial computational cost, introduces additional trade-offs, and requires an accurate initial model (Xu et al., 2006).

A more practical alternative is the so-called “source-independent” method designed to reduce the influence of the source signature on the inversion results. Deconvolution-based trace normalization can be employed in the frequency domain to remove information about the source wavelet from both the recorded and modeled data (Lee and Kim, 2003; Zhou and Greenhalgh, 2003; Seo et al., 2005; Choi and Min, 2012). Choi et al. (2005) propose to define the objective function in the frequency domain by

multiplying the data with the corresponding reference trace. However, the resolution achieved by this deconvolution-based method strongly depends on the signal-to-noise ratio.

Choi and Alkhalifah (2011) define the convolution-based source-independent FWI objective function in the time domain. The first step is to choose a reference trace from both the observed and simulated data sets. Then the simulated data are convolved with the reference trace from the observed data, and the observed data are convolved with the reference trace from the simulated data. The FWI objective function is designed to minimize the difference between these two convolved data sets. One issue with this approach is that the convolution and cross-correlation operations (cross-correlation is used to compute the inversion gradients) tend to generate additional noise, which can be suppressed by applying a time window to the reference traces prior to the convolution (Zhang et al., 2016). Bai and Tsvankin (2019) extend the time-domain source-independent waveform inversion to attenuation estimation using reflection or transmission data from VTI media.

Liu and Tsvankin (2021) develop a time-lapse FWI algorithm for VTI media, and test it using three common strategies for time-lapse FWI (Asnaashari et al., 2015): the parallel-difference (Plessix et al., 2010), sequential-difference, and double-difference techniques (Watanabe et al., 2004; Denli and Huang, 2009). The parallel-difference method uses the same initial model for the baseline and monitor FWI, whereas the sequential-difference method inverts the baseline data to build the initial model for the monitor inversion. The double-difference technique directly estimates the time-lapse parameter variations from the difference between the monitor and baseline data sets.

Time-lapse FWI is particularly sensitive to the accuracy of the source wavelet because of the commonly observed non-repeatability of the source signature between the baseline and monitor surveys. Also, even moderate wavelet-related distortions in the inversion of the baseline and monitor data can lead to large percentage errors in the estimated time-lapse parameter variations. Most existing time-lapse processing algorithms either assume the source wavelet to be known or iteratively estimate it during the inversion. Here, we extend the convolution-based source-independent technique to time-lapse FWI of reflection data from VTI media.

We begin by discussing the methodology of the source-independent FWI technique and outline its application to time-lapse seismic. Analysis of the corresponding objective function is followed by a brief review of the three above-mentioned time-lapse strategies. The derivation of the inversion gradients in terms of the VTI parameters is given in the appendix. The proposed algorithm is applied to the reconstruction of the time-lapse parameter variations in a VTI graben model and in a modified version of the VTI Marmousi model. The inversion results are used to evaluate the robustness of the source-independent algorithm implemented with different time-lapse strategies. We also discuss the influence of the reference trace, time window, and noise on the inverted time-lapse variations.

2 METHODOLOGY OF SOURCE-INDEPENDENT TIME-LAPSE FWI

FWI of time-lapse data involves the inversion of the baseline and monitor surveys. The baseline survey is acquired before hydrocarbon production or CO_2 injection, and the monitor survey during or after production/injection. Typically, FWI is first applied to the baseline data to obtain the baseline model. Then the monitor survey is processed using different approaches according to the chosen time-lapse strategy. The subtraction of the inverted baseline model from the monitor model yields the time-lapse parameter variations.

Conventional algorithms use the L_2 -norm objective function (e.g., Tarantola, 1984) for the inversion of the baseline (subscript b) data:

$$S_b(\mathbf{m}_b) = \frac{1}{2} \left\| \left[\mathbf{d}_b^{\text{sim}}(\mathbf{m}_b) - \mathbf{d}_b^{\text{obs}} \right] \right\|^2 = \frac{1}{2} \left\| \left[\mathbf{G}^{\text{sim}} * \mathbf{s}^{\text{sim}} - \mathbf{G}^{\text{obs}} * \mathbf{s}^{\text{obs}} \right] \right\|^2, \quad (1)$$

where $\mathbf{d}_b^{\text{sim}}$ is the data simulated for the baseline model \mathbf{m}_b , $\mathbf{d}_b^{\text{obs}}$ is the observed baseline data, the sign “*” denotes convolution, and \mathbf{G}^{sim} and \mathbf{G}^{obs} are the simulated and actual Green’s functions.

2.1 Source-independent methodology

To reduce the influence of the source wavelet, Choi and Alkhalifah (2011) and Zhang et al. (2016) propose the following convolution-based source-independent objective function in the time domain:

$$\begin{aligned} S_b(\mathbf{m}_b) &= \frac{1}{2} \left\| \left[\mathbf{d}_b^{\text{sim}}(\mathbf{m}_b) * \left(W \mathbf{d}_{\text{ref}}^{\text{obs}} \right) - \mathbf{d}_b^{\text{obs}} * \left(W \mathbf{d}_{\text{ref}}^{\text{sim}} \right) \right] \right\|^2 \\ &= \frac{1}{2} \left\| \left[\mathbf{G}^{\text{sim}} * \mathbf{s}^{\text{sim}} * W \mathbf{G}_{\text{ref}}^{\text{obs}} * \mathbf{s}^{\text{obs}} - \mathbf{G}^{\text{obs}} * \mathbf{s}^{\text{obs}} * W \mathbf{G}_{\text{ref}}^{\text{sim}} * \mathbf{s}^{\text{sim}} \right] \right\|^2 \\ &= \frac{1}{2} \left\| \left[\tilde{\mathbf{G}}^{\text{s}} * \tilde{\mathbf{s}}^{\text{c}} - \tilde{\mathbf{G}}^{\text{o}} * \tilde{\mathbf{s}}^{\text{c}} \right] \right\|^2, \end{aligned} \quad (2)$$

where $W = W(t)$ is the chosen time window, and \mathbf{d}_{ref} denotes the reference trace. $\mathbf{G}_{\text{ref}}^{\text{obs}}$ and $\mathbf{G}_{\text{ref}}^{\text{sim}}$ are the Green's functions for the reference traces, $\tilde{\mathbf{G}}^{\text{s}}$ and $\tilde{\mathbf{G}}^{\text{o}}$ are the Green's functions for the new convolution-based simulated and observed data, and $\tilde{\mathbf{s}}^{\text{c}}$ is the new source wavelet. The expressions for $W(t)$, $\tilde{\mathbf{G}}^{\text{s}}$, $\tilde{\mathbf{G}}^{\text{o}}$, and $\tilde{\mathbf{s}}^{\text{c}}$ are:

$$\text{Time window : } W(t) = \begin{cases} 1 & t_l \leq t \leq t_h; \\ 0 & \text{otherwise.} \end{cases} \quad (3)$$

$$\text{New Green's functions : } \begin{cases} \tilde{\mathbf{G}}^{\text{s}} = \mathbf{G}^{\text{sim}} * W \mathbf{G}_{\text{ref}}^{\text{obs}}; \\ \tilde{\mathbf{G}}^{\text{o}} = \mathbf{G}^{\text{obs}} * W \mathbf{G}_{\text{ref}}^{\text{sim}}. \end{cases} \quad (4)$$

$$\text{New source wavelet : } \tilde{\mathbf{s}}^{\text{c}} = \mathbf{s}^{\text{sim}} * \mathbf{s}^{\text{obs}}; \quad (5)$$

t_l and t_h are the boundaries of the time window applied to the reference trace.

The new simulated and observed data in equation 2 could be expressed as the convolutions of the new Green's functions ($\tilde{\mathbf{G}}^{\text{s}}$ and $\tilde{\mathbf{G}}^{\text{o}}$) and the source wavelet ($\tilde{\mathbf{s}}^{\text{c}}$). Because the wavelet $\tilde{\mathbf{s}}^{\text{c}}$ is the same for the simulated and observed data, the deviation of the estimated source signature from the actual wavelet is theoretically eliminated from the modified objective function.

The time window $W(t)$ is used to mitigate the artifacts caused by the convolution and cross-correlation operations. To save computing time and ensure efficient noise suppression, the time window should be as short as possible but has to contain sufficient information about the source wavelet. Zhang et al. (2016) suggest that the lower cut-off time (t_l) should be before the first arrival, and the window should contain at least one full waveform, such as the P-wave direct arrival. Here, we define the time window using the Butterworth filter:

$$W(t) = \frac{1}{1 + \left(\frac{t-t_l}{t_h}\right)^{2n}} = \frac{1}{1 + \left(\frac{t-t_l}{t_h}\right)^{30}}, \quad (6)$$

where n is the order of the filter ($n = 15$ in our examples).

2.2 Implementation of time-lapse FWI

We parameterize VTI media by the velocities V_{P0} (P-wave vertical velocity), V_{S0} (S-wave vertical velocity), $V_{\text{hor,P}}$ (P-wave horizontal velocity), $V_{\text{nm0,P}}$ (P-wave normal-moveout velocity from a horizontal reflector), and density ρ (Tsvankin, 2012; Alkhalifah and Plessix, 2014; Kamath and Tsvankin, 2016). Multicomponent data are simulated by solving the 2D wave equation for elastic, arbitrarily heterogeneous VTI media with a fourth-order finite-difference algorithm (Singh et al., 2018). The gradient of the objective function with respect to the medium parameters is derived in Appendix A using the adjoint-state method (e.g., Choi and Alkhalifah, 2011; Kamath and Tsvankin, 2013; Singh et al., 2019).

The time-lapse strategies employed here use the same objective function for the baseline inversion but differ in handling the monitor survey (or the time-lapse data difference). In the parallel-difference approach (Plessix et al., 2010), the baseline and monitor inversions are performed independently but with the same initial model. The time-lapse model produced by this method can remain sufficiently accurate when the errors in the inverted baseline and monitor models are similar. The sequential-difference strategy (Asnaashari et al., 2012) uses the inversion of the baseline data to build the initial model for FWI of the monitor survey. This facilitates the convergence of the monitor inversion due to the similarity between the baseline and monitor surveys.

In the double-difference method (Denli and Huang, 2009), the monitor inversion operates directly on the difference between the monitor and baseline data ($\mathbf{d}_{\text{m}}^{\text{obs}} - \mathbf{d}_{\text{b}}^{\text{obs}}$). The monitor model is obtained by minimizing the difference $\Delta \mathbf{d}$ between the simulated monitor data $\mathbf{d}_{\text{m}}^{\text{sim}}$ and the ‘‘composite’’ data \mathbf{d}_{com} , starting from the inverted baseline model:

$$\Delta \mathbf{d} = (\mathbf{d}_{\text{m}}^{\text{obs}} - \mathbf{d}_{\text{b}}^{\text{obs}}) - (\mathbf{d}_{\text{m}}^{\text{sim}} - \mathbf{d}_{\text{b}}^{\text{sim}}) = \mathbf{d}_{\text{com}} - \mathbf{d}_{\text{m}}^{\text{sim}}, \quad (7)$$

$$\mathbf{d}_{\text{com}} = \mathbf{d}_{\text{m}}^{\text{obs}} - \mathbf{d}_{\text{b}}^{\text{obs}} + \mathbf{d}_{\text{b}}^{\text{sim}}, \quad (8)$$

where $\mathbf{d}_{\text{b}}^{\text{sim}}$ is the data simulated for the inverted baseline model.

3 SYNTHETIC EXAMPLES

The developed source-independent TLFWI algorithm is tested on a VTI graben model and the modified VTI Marmousi model. The synthetic data for both models are generated with the Ricker wavelet (Figure 1a). The source-independent algorithm is applied for two distorted wavelets (Figures 1b, 1c) used in the inversion. FWI is implemented using the multiscale approach with four frequency bands (Singh et al., 2019; Liu and Tsvankin, 2021). Frequencies below 2 Hz are not included in the inversion to make

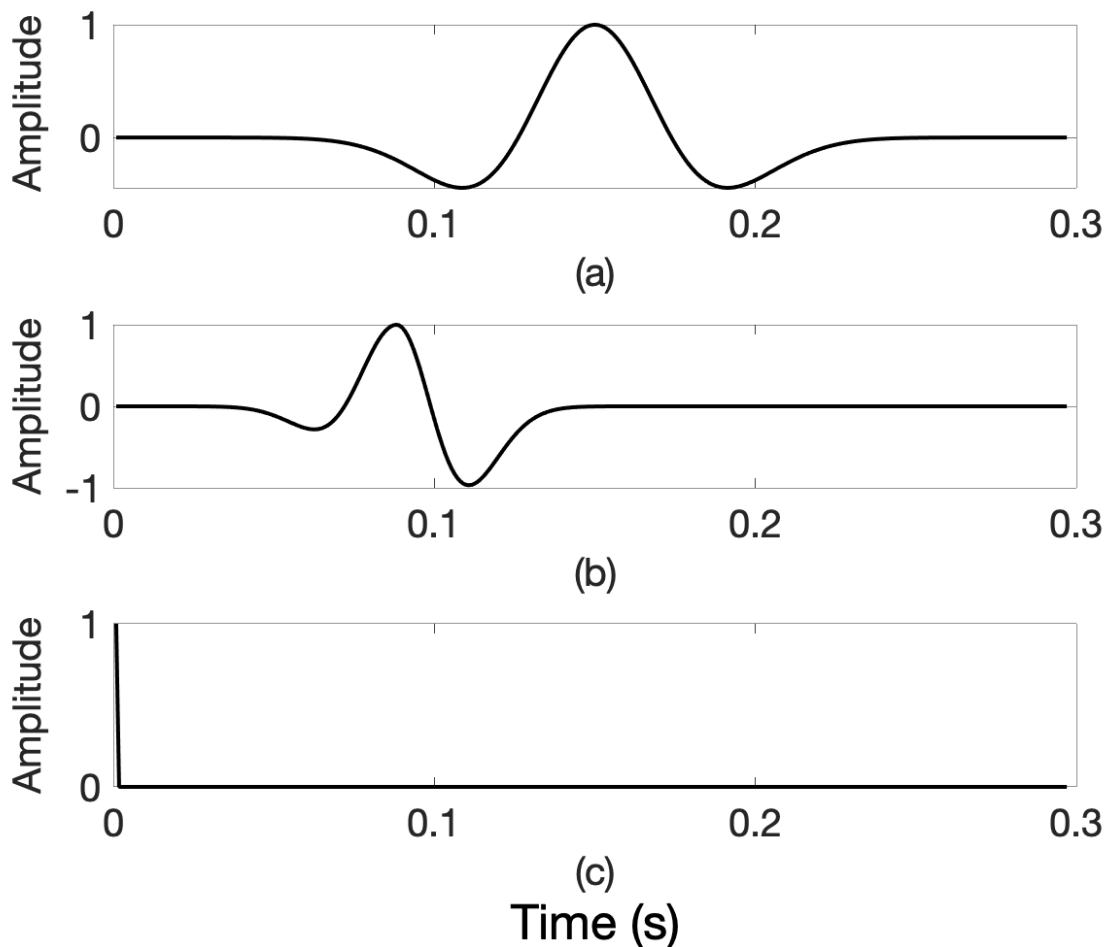


Figure 1. Source wavelets used in the synthetic examples: (a) the Ricker wavelet with a central frequency of 10 Hz (actual wavelet), (b) the distorted “Ricker” wavelet with a central frequency of 17 Hz (Wavelet 1), and (c) the spike (Wavelet 2).

the examples more realistic.

3.1 VTI graben model

The elastic wavefield is excited by 58 shots (point explosions) placed with a constant increment (80 m) along a horizontal line at a depth of 40 m (Figure 2a). We employ 400 receivers evenly distributed with an increment of 10 m along the horizontal line at a depth of 100 m (Figure 2a). The medium parameters for the monitor survey (Liu and Tsvankin, 2021) are obtained by reducing the baseline vertical velocities V_{P0} and V_{S0} in the target area (i.e., in the dipping layer segments) by approximately 13%, and density ρ by 10% (Figure 2). The initial baseline models (Figure 2b, 2e, 2h, 2k, 2n) are computed by Gaussian smoothing of the actual parameter distributions. The benchmark time-lapse results (Figure 3) are obtained by performing FWI with the actual wavelet following the parallel-difference strategy. The time-lapse parameter variations inside the “reservoir” are well estimated and there are no significant artifacts outside the target zone. The artifacts near the boundaries of the graben structure are caused primarily by edge effects in the L_2 -norm objective function. Next, the conventional FWI algorithm is applied to the baseline data using a distorted source wavelet (Wavelet 1). The incorrect source signature completely corrupts the inversion results, and even the graben structure itself is barely visible (Figure 4). It is clear that conventional FWI is unable to reconstruct the time-lapse parameter changes for the distorted wavelet. Then we apply the source-independent FWI algorithm using Wavelet 1. After estimating the baseline model,

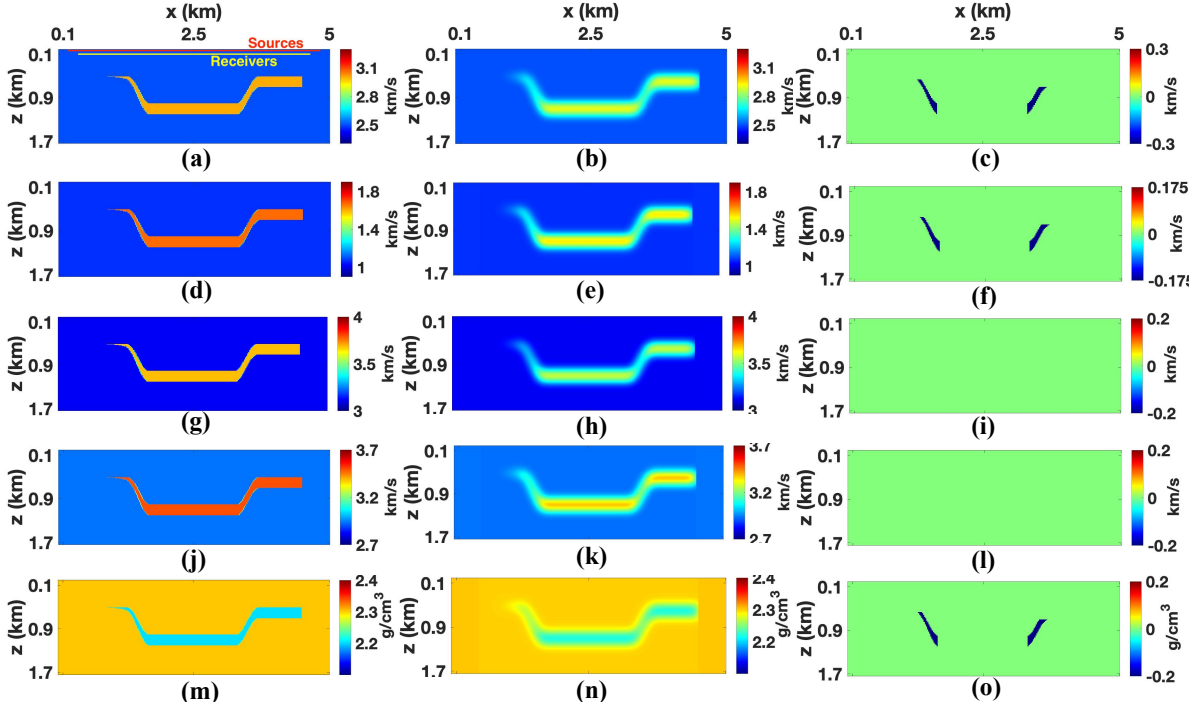


Figure 2. Parameters of the baseline graben model with a grid size of 10×10 m: (a) the P-wave vertical velocity (V_{P0}), (d) the S-wave vertical velocity (V_{S0}), (g) the P-wave horizontal velocity ($V_{hor,P}$), (j) the P-wave normal-moveout velocity ($V_{nmo,P}$), and (m) the density (ρ). The initial baseline model of: (b) V_{P0} , (e) V_{S0} , (h) $V_{hor,P}$, (k) $V_{nmo,P}$, and (n) ρ . The actual time-lapse differences for (c) V_{P0} , (f) V_{S0} , (i) $V_{hor,P}$, (l) $V_{nmo,P}$, and (o) ρ .

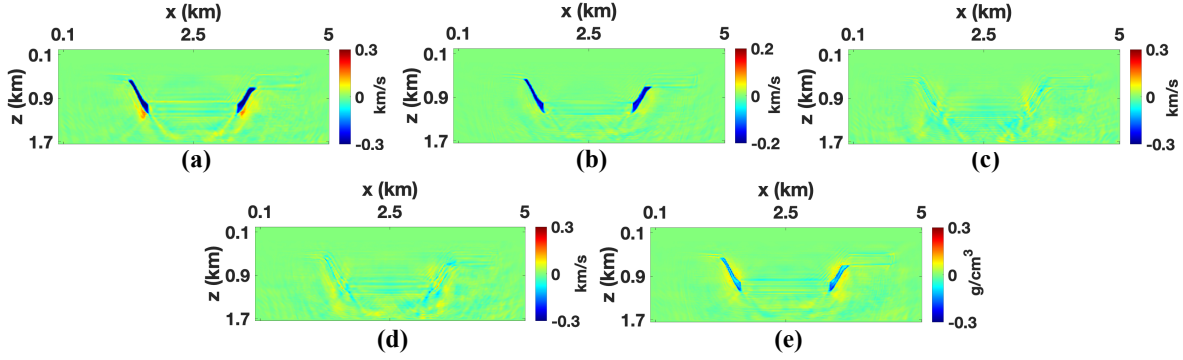


Figure 3. Time-lapse parameter variations obtained by conventional FWI with the actual wavelet using the parallel-difference method (benchmark results): (a) V_{P0} , (b) V_{S0} , (d) $V_{hor,P}$, (e) $V_{nmo,P}$, and (c) ρ .

three time-lapse methods are used to reconstruct the parameter variations (note that the P-wave NMO and horizontal velocities are held constant). The selected reference traces for both the vertical and horizontal particle velocities correspond to the receiver located closest to the source, which ensures high fidelity of the source signal.

3.1.1 Parallel- and sequential-difference methods

The time-lapse changes estimated by source-independent FWI using the parallel- and sequential-difference strategies are sufficiently close to the benchmark results (Figure 2), although the amplitude of the time-lapse anomalies is slightly underestimated. Also, our method generates some false time-lapse anomalies in the velocities $V_{hor,P}$ and $V_{nmo,P}$ because of the parameter trade-offs (Figures 5d, 5e, 5g, 5h). The performance of the parallel-difference (Figures 5a, 5d, 5m) and sequential-difference (Figures 5b, 5e, 5n)

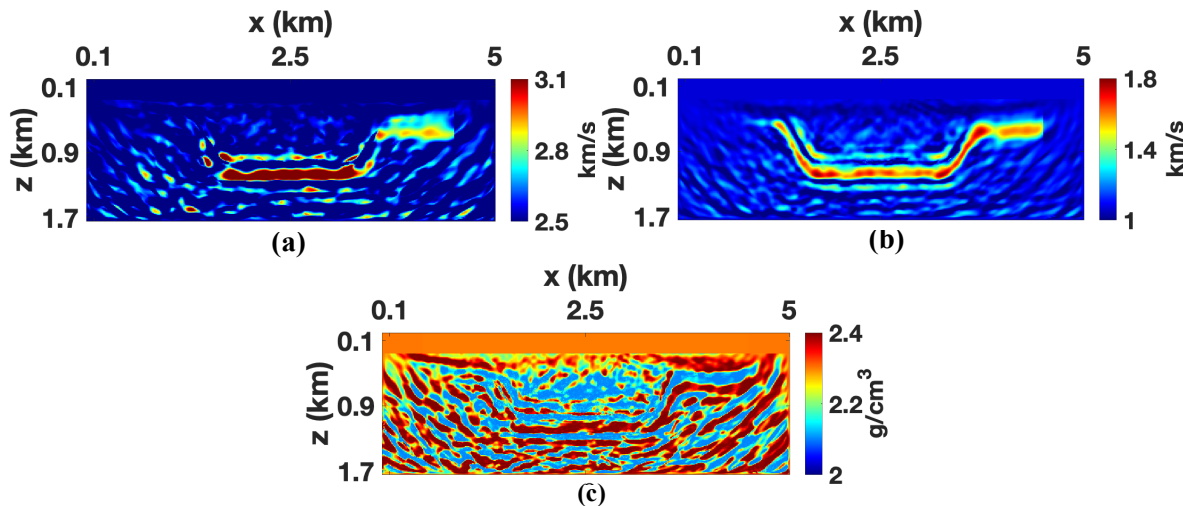


Figure 4. Baseline models estimated by conventional FWI using Wavelet 1: (a) V_{P0} , (b) V_{S0} , and (c) ρ .

methods in reconstructing the time-lapse variations in V_{P0} , V_{S0} , and ρ and suppressing the artifacts is comparable. The robustness of our algorithm applied with the parallel-difference method is further evaluated in Figure 6 for the spike wavelet that represents an extreme shape distortion. Still, the time-lapse changes of the parameters V_{P0} , V_{S0} , and ρ are reconstructed with sufficient resolution similar to that for Wavelet 1 (Figures 5a, 5d, 5m). Clearly, our source-independent algorithm can handle even extreme frequency and shape distortions in the source wavelet for high-quality multicomponent data.

3.1.2 Double-difference method

Although the double-difference method does not produce significant false anomalies, the reconstructed temporal variations in V_{P0} , V_{S0} , and ρ have the wrong sign (Figures 5c, 5f, 5o). In contrast to the other two strategies, this method operates with the “composite” data ($\mathbf{d}_m^{\text{obs}} - \mathbf{d}_b^{\text{obs}} + \mathbf{d}_b^{\text{sim}}$) generated by adding the wavefield simulated for the inverted baseline model to the actual time-lapse data difference (equations 7 and 8). The frequency distortion of Wavelet 1 leads to a phase mismatch between the simulated baseline data $\mathbf{d}_b^{\text{sim}}$ and the observed wavefield. The resulting degradation of the “composite” data set prevents the source-independent algorithm from producing a sufficiently accurate monitor model.

To verify this conjecture, in Figure 7b we use a wavelet which has the shape of Wavelet 1 but correct frequency to simulate the baseline seismograms and generate the “composite” data. The monitor inversion is still performed using the source-independent algorithm with Wavelet 1. In this case, the reconstructed parameter variations in the target area have the correct sign (Figure 7b) and are sufficiently close to the benchmark results. Evidently, the double-difference method has to be applied with a wavelet that has an accurate frequency to properly estimate the temporal parameter variations. If the data for the inverted baseline model are simulated using the actual wavelet (FWI is still performed with Wavelet 1), the double-difference method (Figure 7c) produces the time-lapse changes in the velocity V_{P0} with higher resolution than the other two methods (Figures 5a, 5b). One possible solution to at least partially resolve the issue with errors in the simulated baseline data generated with a distorted wavelet is to apply dynamic warping. That method has been proposed for time-shift estimation in time-lapse processing by matching traces from the baseline and monitor surveys using the criterion of minimal dissimilarity (Rickett et al., 2007; Hale, 2013; Venstad, 2014; Holschuh et al., 2014; Li et al., 2019). We will investigate this method as part of our future research in anisotropic time-lapse FWI.

3.1.3 Influence of noise

Next, the data are contaminated with Gaussian noise that has the signal-to-noise ratio equal to 16. We employ only the parallel-difference method due to its general robustness for noisy data (Liu and Tsvankin, 2021). Here we show only the parameters V_{P0} , V_{S0} , and ρ reconstructed by conventional FWI using the actual source wavelet (benchmark results) and by the source-independent algorithm using the two distorted wavelets.

The baseline models (especially V_{P0}) inverted by the source-independent algorithm using Wavelet 1 are somewhat distorted, likely due to the noise amplification in the convolution and cross-correlation operations. However, the source-independent algorithm

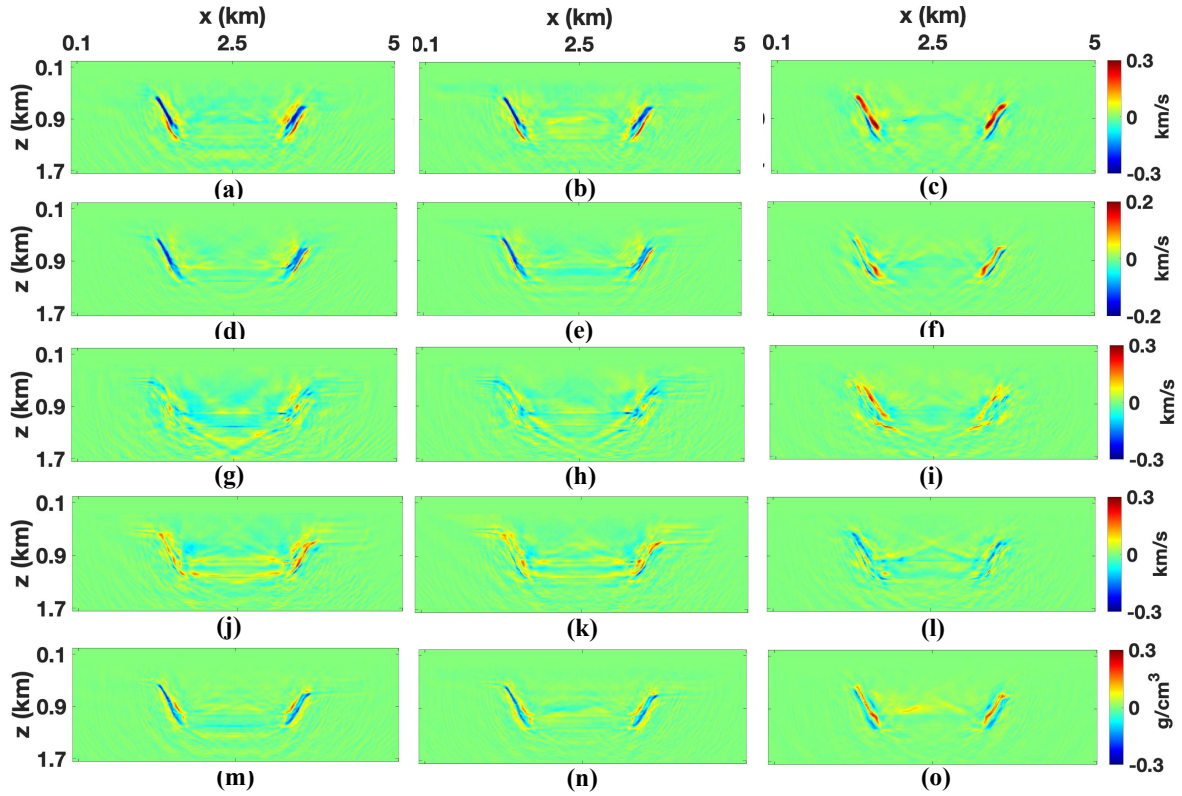


Figure 5. Time-lapse parameter variations reconstructed by the source-independent algorithm with Wavelet 1. The parallel-difference method: (a) V_{P0} , (d) V_{S0} , (g) $V_{hor,P}$, (j) $V_{nmo,P}$, and (m) ρ . The sequential-difference method: (b) V_{P0} , (e) V_{S0} , (h) $V_{hor,P}$, (k) $V_{nmo,P}$, and (n) ρ . The double-difference method: (c) V_{P0} , (f) V_{S0} , (i) $V_{hor,P}$, (l) $V_{nmo,P}$, and (o) ρ .

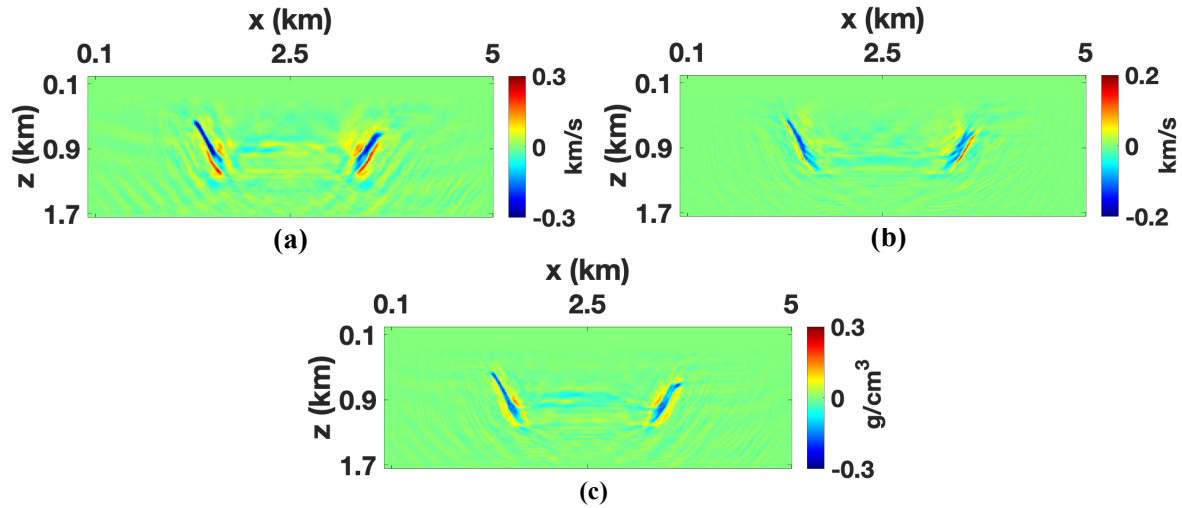


Figure 6. Time-lapse parameter variations estimated by the source-independent algorithm with the spike wavelet (Wavelet 2) using the parallel-difference method: (a) V_{P0} , (b) V_{S0} , and (c) ρ .

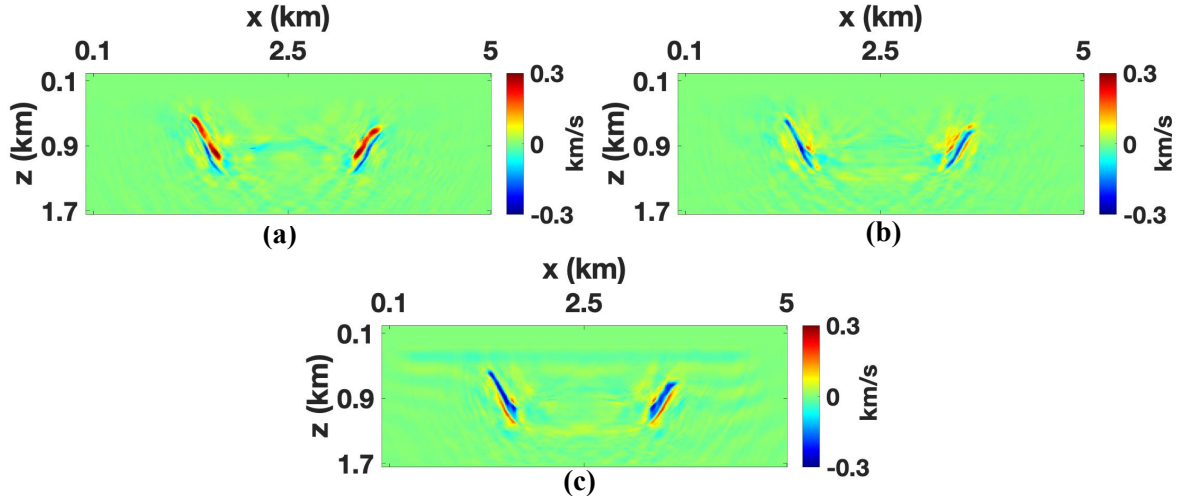


Figure 7. Time-lapse variations of the velocity V_{P0} reconstructed by the source-independent algorithm using the double-difference method. FWI is performed with Wavelet 1, whereas the data for the inverted baseline model (d_b^{sim}) are generated with: (a) Wavelet 1, (b) a signal that has the shape of Wavelet 1 but correct frequency, (c) the actual wavelet.

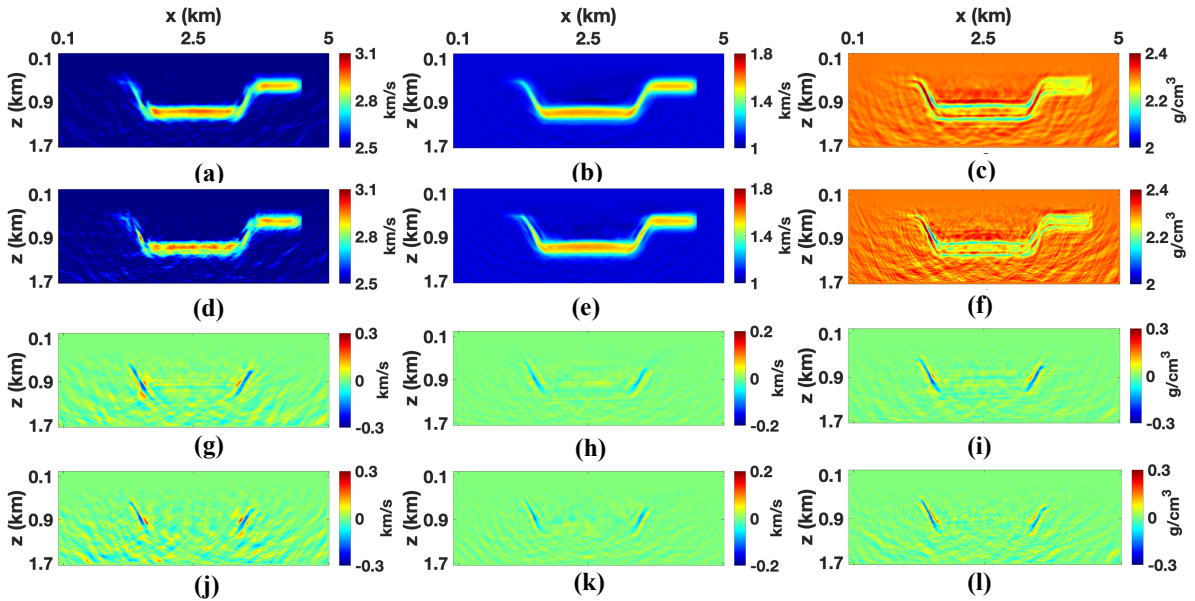


Figure 8. Inverted baseline models and time-lapse variations obtained from noisy data (signal-to-noise ratio is 16). Inverted baseline models obtained by conventional FWI with the actual wavelet [(a) V_{P0} , (b) V_{S0} , (c) ρ] and by the source-independent FWI with Wavelet 1 [(d) V_{P0} , (e) V_{S0} , (f) ρ]. Time-lapse variations obtained by conventional FWI with the actual wavelet [(g) V_{P0} , (h) V_{S0} , (i) ρ] and by the source-independent FWI with Wavelet 1 [(j) V_{P0} , (k) V_{S0} , (l) ρ].

(Figures 8d, 8e) surprisingly produces a slightly more accurate reconstruction of the baseline velocities in the “reservoir” compared to conventional FWI applied with the actual wavelet (Figures 8a, 8b). Still, the time-lapse variations of V_{P0} estimated by our algorithm (Figure 8j) have a somewhat lower resolution than the benchmark section (Figure 8g). Nevertheless, the changes in the velocity V_{S0} reconstructed by the source-independent FWI (Figure 8k) are close to those obtained with the actual wavelet (Figure 8h). There is no significant difference between the accuracy of the time-lapse results produced with Wavelet 1 and the spike wavelet (Wavelet 2; not shown). This test indicates that our algorithm not only can handle significant wavelet distortions but also reconstruct the temporal parameter variations for data contaminated with moderate noise.

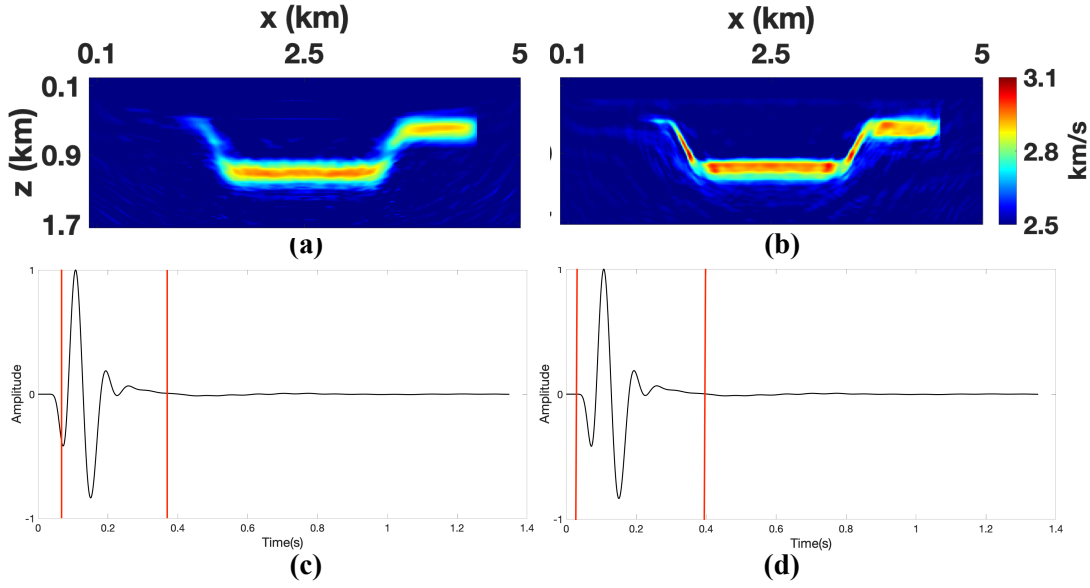


Figure 9. Velocity V_{P0} estimated by the source-independent algorithm from the baseline data for the graben model using the spike wavelet and two time windows: (a) window 1 [plot(c)] and (b) window 2 [plot(d)].

3.1.4 Influence of the reference trace and time window

The objective function for the source-independent FWI (equation 2) is sensitive to the choice of the reference trace and time window. Our results show that employing a reference trace that represents the average of several near-offset traces produces smaller errors compared to using the zero-offset trace; the worst results are obtained using a far-offset trace. This is not surprising because of the higher data fidelity close to the source (Xu et al., 2006; Choi and Alkhalifah, 2011; Zhang et al., 2016). Note that an arrival-time (moveout) correction needs to be applied to the near-offset traces to ensure their in-phase stacking in generating the reference trace.

As mentioned above, time windowing mitigates the artifacts (noise) caused by the convolution and cross-correlation operations. However, the reference trace may not contain enough information about the source signal if the window is too narrow. Figure 9 shows the velocity V_{P0} reconstructed from the baseline data for the graben model. The source-independent FWI is applied with the spike wavelet and two different time windows. If the window does not capture the entire first arrival (Figure 9c), the graben structure is poorly resolved because the reference trace does not provide sufficient information about the wavelet (Figure 9a). The section in Figure 9b is also suboptimal because the time window is too wide (Figure 9d), which results in additional noise produced by convolution and cross-correlation. This observation is consistent with the conclusions of Zhang et al. (2016). Therefore, the time window in our tests is chosen to contain the full waveform of the first arrival (such as the direct P-wave).

3.2 VTI Marmousi model

Next, we apply our algorithm to the modified VTI Marmousi model (Figure 10). The source/receiver geometry is the same as that for the graben model but the receivers are at a depth of 230 m. The time-lapse parameters for the monitor survey are obtained by reducing the baseline vertical velocities V_{P0} , V_{S0} and density ρ in the target area (between the depths of 870 m and 1100 m) by 15% (Figures 10c, 10f, 10o). The reference trace used in the source-independent algorithm is recorded 70 m away from the source. As before, elastic FWI is applied to the vertical and horizontal particle-velocity components. After generating the observed data using the actual wavelet, the benchmark parameter changes are obtained by the conventional FWI algorithm using the parallel-difference method with the actual wavelet (Figure 11). Despite the model complexity and small thickness of the “reservoir,” the time-lapse variations are reconstructed with sufficiently high resolution. Next, we perform conventional FWI of the baseline data using Wavelet 1. However, the inversion becomes unstable and does not converge, likely due to the increased sensitivity to wavelet distortions for this structurally complex model. Then we employ a wavelet with the same shape distortion as Wavelet 1 but correct frequency. Still, the geologic structure is not properly resolved in the inverted baseline models (Figure 12), and it is obvious that conventional FWI is incapable of reconstructing the time-lapse changes with the inaccurate wavelet. Because of the problems with

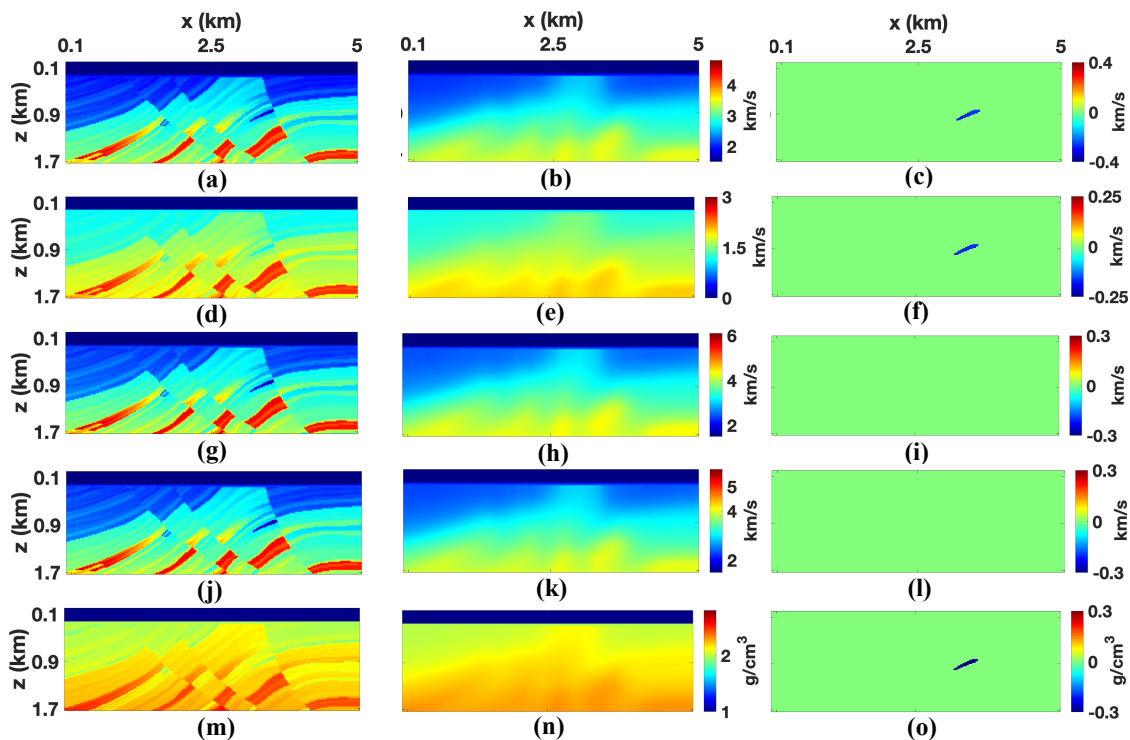


Figure 10. Baseline parameters of the modified VTI Marmousi model with a grid size of 10×10 m: (a) V_{P0} , (d) V_{S0} , (g) $V_{hor,P}$, (j) $V_{nmo,P}$, and (m) ρ . The initial baseline model of: (b) V_{P0} , (e) V_{S0} , (h) $V_{hor,P}$, (k) $V_{nmo,P}$, and (n) ρ . The actual time-lapse differences for (c) V_{P0} , (f) V_{S0} , (i) $V_{hor,P}$, (l) $V_{nmo,P}$, and (o) ρ .

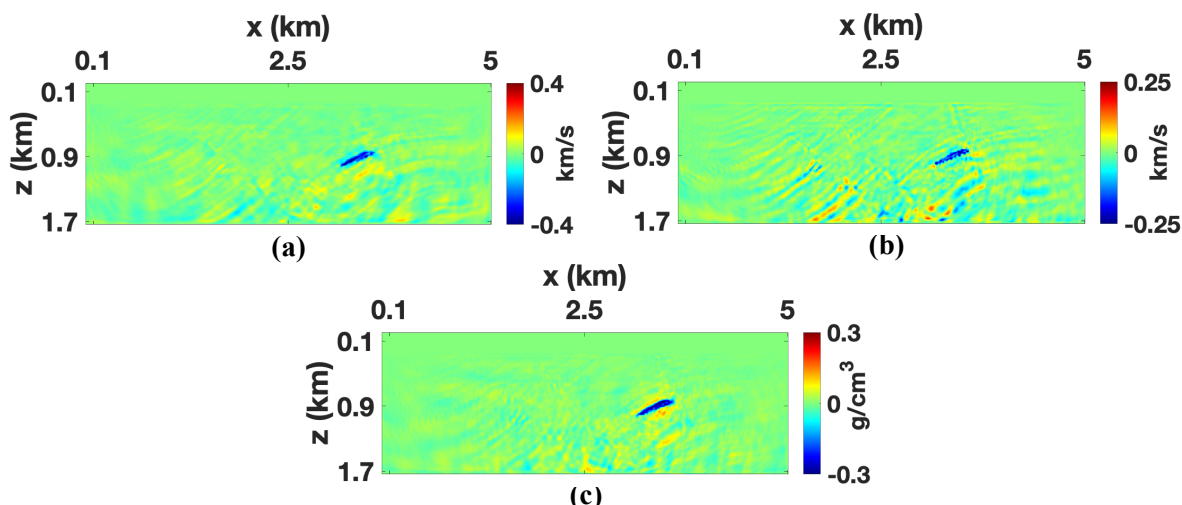


Figure 11. Time-lapse variations for the Marmousi model obtained by conventional FWI using the parallel-difference method with the actual wavelet (benchmark results): (a) V_{P0} , (b) V_{S0} , and (c) ρ .

the double-difference method discussed above, the source-independent algorithm is applied only with the other two strategies using the same distorted wavelet (Wavelet 1). In contrast to the graben model, the sequential-difference method (Figures 13b, 13d, 13f) reconstructs the temporal variations with higher resolution and fewer artifacts than the parallel-difference method (Figures 13a, 13c, 13e).

Clearly, the performance of these methods varies with the model complexity. Because FWI is a local optimization technique, it converges toward the minimum of the objective function closest to the initial model. The convolution operations in the source-

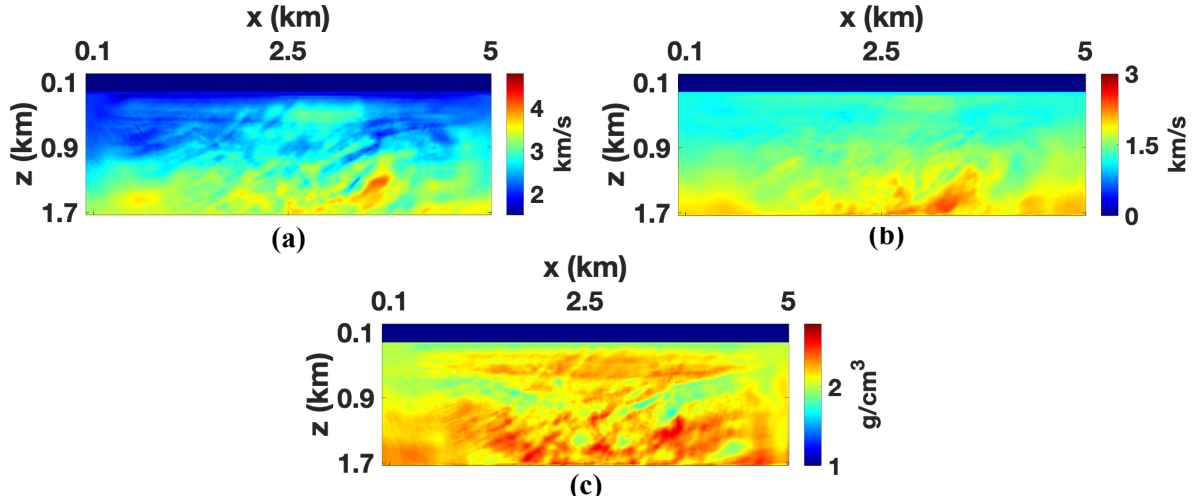


Figure 12. Baseline Marmousi models produced by conventional FWI using a wavelet with only a shape distortion: (a) V_{P0} , (b) V_{S0} , and (c) ρ .

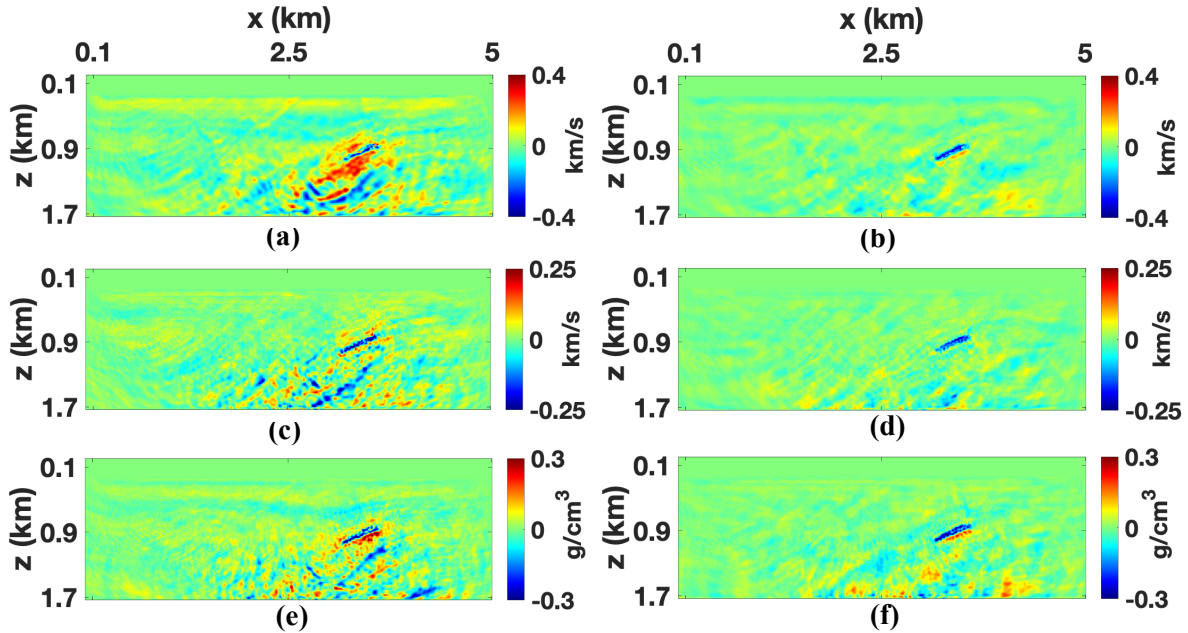


Figure 13. Time-lapse parameter variations for the Marmousi model obtained by the source-independent algorithm with Wavelet 1. The parallel-difference method: (a) V_{P0} , (c) V_{S0} , and (e) ρ . The sequential-difference method: (b) V_{P0} , (d) V_{S0} , and (f) ρ .

independent method make the shape of the objective function more complex, and the pronounced heterogeneity of the Marmousi model increases the inversion nonlinearity. Starting with the inverted baseline model (which is relatively close to the monitor model) in the sequential-difference method improves the convergence toward the monitor model, which yields more accurate time-lapse variations (Figures 13b, 13d, 13f). Comparison of the output of the source-independent FWI applied with the sequential-difference method (Figures 13b, 13d, 13f) and the benchmark results (Figure 11) shows that despite the combination of the significantly distorted wavelet and pronounced heterogeneity, our algorithm reconstructs the time-lapse variations with acceptable resolution. The somewhat lower accuracy of the source-independent technique (as well as additional artifacts) for the Marmousi model as compared to the graben structure is likely due to the increased medium complexity. In particular, multiple reflections, which could be captured by the time window used in the convolution operations, may hinder the convergence of the algorithm.

4 CONCLUSIONS

We implemented a “source-independent” time-lapse FWI algorithm for VTI media in the time domain. The modified FWI objective function is designed to mitigate the dependence of the inverted parameters on the accuracy of the source wavelet by employing two additional data sets obtained by convolution operations. Our testing shows that the reference traces used in the convolutions should be located near the source. The convolution time window is chosen to include the entire first arrival (e.g., the direct P-wave) to ensure that the reference trace contains sufficient source information.

The synthetic examples demonstrate that the developed source-independent algorithm can accurately reconstruct the time-lapse variations even for significantly distorted source signals (such as the spike wavelet). The testing also confirms the ability of the method to deal with noisy data and strongly heterogeneous media, although the results for the Marmousi model are somewhat inferior to those for the simpler graben structure. The source-independent technique is particularly important in time-lapse processing because it can handle the non-repeatability of the source wavelet.

5 ACKNOWLEDGMENTS

We thank the members of the Anisotropy-Team at the Center for Wave Phenomena (CWP) at Colorado School of Mines for useful discussions. This work is supported by the Consortium Project on Seismic Inverse Methods for Complex Structures at CWP.

6 APPENDIX A

7 INVERSION GRADIENTS FOR THE SOURCE-INDEPENDENT FWI

Starting with Choi and Alkhalifah (2011), several publications discuss the “source-independent” FWI in the time domain, but none of these papers (e.g., Zhang et al., 2016; Bai and Tsvankin, 2019) presents explicit expressions for the inversion gradients. Here, we follow the approach in Kamath and Tsvankin (2016) to derive the gradients of the objective function with respect to the VTI parameters. The source-independent technique makes the objective function and the generation of the back-propagated wavefield more complex.

The objective function (equation 2) is minimized under the constraint that the modeled displacement $\mathbf{d}^{\text{sim}}(\mathbf{x}_r, t)$ satisfies the elastic wave equation (Plessix, 2006; Liu and Tromp, 2006). For arbitrarily anisotropic, heterogeneous media, the wave equation can be written as:

$$\rho \frac{\partial^2 d_i^{\text{sim}}}{\partial t^2} - \frac{\partial}{\partial x_j} \left(c_{ijkl} \frac{\partial d_k^{\text{sim}}}{\partial x_l} \right) = f_i, \quad (\text{A-1})$$

where \mathbf{d} is displacement field, ρ is the density, \mathbf{f} is the density of the body forces, and c_{ijkl} ($i, j, k, l = 1, 2, 3$) are the stiffness coefficients.

The displacement is subject to the initial conditions,

$$\mathbf{d}^{\text{sim}}(\mathbf{x}, 0) = 0, \quad \frac{\partial \mathbf{d}^{\text{sim}}(\mathbf{x}, 0)}{\partial t} = 0, \quad (\text{A-2})$$

and the radiation boundary condition,

$$\mathbf{d}^{\text{sim}}(\mathbf{x}, t)|_{\mathbf{x} \rightarrow \infty} \rightarrow 0. \quad (\text{A-3})$$

Adopting the Lagrange multiplier method, we can define the Lagrangian Δ as:

$$\begin{aligned} \Delta = & \frac{1}{2} \sum_r \int_0^T \|\mathbf{d}^{\text{sim}}(\mathbf{x}, t) * W \mathbf{d}_{\text{ref}}^{\text{obs}}(\mathbf{x}_f, t) - \mathbf{d}^{\text{obs}}(\mathbf{x}, t) * W d_{\text{ref}}^{\text{sim}}(\mathbf{x}_f, t)\|^2 dt \\ & - \int_0^T \int_{\Omega} \lambda_i \left[\rho \frac{\partial^2 d_i^{\text{sim}}}{\partial t^2} - \frac{\partial}{\partial x_j} \left(c_{ijkl} \frac{\partial u_k}{\partial x_l} \right) - f_i \right] dV dt, \end{aligned} \quad (\text{A-4})$$

where Ω is the integration domain (volume), and $\Lambda(\mathbf{x}, t)$ is the yet unknown vector Lagrangian multiplier. After intergration by parts and application of the Gaussian divergence theorem, the change in the Lagrangian can be found in the following form:

$$\delta \Delta = - \int_0^T \sum_{r=1}^N \left[d_i^{\text{sim}}(\mathbf{x}, t) * d_{\text{ref}}^{\text{obs}}(\mathbf{x}_f, t) - d_i^{\text{obs}}(\mathbf{x}, t) * d_{\text{ref}}^{\text{sim}}(\mathbf{x}_f, t) \right] d_i^{\text{obs}}(\mathbf{x}, t) \delta(\mathbf{x} - \mathbf{x}_r) \delta d_{\text{ref}}^{\text{sim}}(\mathbf{x}_f, t) dt$$

$$\begin{aligned}
& \int_0^T \int_{\Omega} \sum_{r=1}^N \left[d_i^{\text{sim}}(\mathbf{x}, t) * d_{\text{ref}}^{\text{obs}}(\mathbf{x}_f, t) - d_i^{\text{obs}}(\mathbf{x}, t) * d_{\text{ref}}^{\text{sim}}(\mathbf{x}_f, t) \right] d_{\text{ref}}^{\text{obs}}(\mathbf{x}_f, t) \delta(\mathbf{x} - \mathbf{x}_r) \delta d_i^{\text{sim}}(\mathbf{x}, t) dV dt \\
& - \int_0^T \int_{\Omega} \delta c_{ijkl} \frac{\partial d_k^{\text{sim}}}{\partial x_l} \frac{\partial \lambda_i}{\partial x_j} dV dt - \int_0^T \int_{\Omega} \left[\rho \frac{\partial^2 \lambda_i}{\partial t^2} - \frac{\partial}{\partial x_j} \left(c_{ijkl} \frac{\partial \lambda_k}{\partial x_l} \right) \right] \delta d_i^{\text{sim}} dV dt \\
& - \int_{\Omega} \left[\rho \lambda_i \frac{\partial (\delta d_i^{\text{sim}})}{\partial t} - \rho \delta d_i^{\text{sim}} \frac{\partial \lambda_i}{\partial t} \right]_0^T dV \\
& + \int_0^T \int_{\partial\Omega} \lambda_i \left[\delta c_{ijkl} \frac{\partial d_k^{\text{sim}}}{\partial x_l} + c_{ijkl} \frac{\partial (\delta d_k^{\text{sim}})}{\partial x_l} \right] n_j dS dt - \int_0^T \int_{\partial\Omega} \delta d_i^{\text{sim}} c_{ijkl} \frac{\partial \lambda_k}{\partial x_l} n_j dS dt,
\end{aligned} \tag{A-5}$$

where $\partial\Omega$ is the surface of Ω , \mathbf{n} is the vector normal to $\partial\Omega$, and $r = 1, 2, 3 \dots N$ denotes the receivers. Following Choi and Alkhalifah (2011), the second term on the right-hand side of equation A-5 can be ignored because it operates with only the reference trace. Perturbing $\mathbf{d}^{\text{sim}}(\mathbf{x}, t)$ in equations A-2 and A-3 yields the initial and boundary conditions for $\delta \mathbf{d}^{\text{sim}}(\mathbf{x}, t)$:

$$\delta \mathbf{d}^{\text{sim}}(\mathbf{x}, 0) = 0, \quad \frac{\partial \delta \mathbf{d}^{\text{sim}}(\mathbf{x}, 0)}{\partial t} = 0, \quad \delta \mathbf{d}^{\text{sim}}(\mathbf{x}, t)|_{\mathbf{x} \rightarrow \infty} \rightarrow 0. \tag{A-6}$$

The wavefield λ is then constrained by the ‘‘final’’ states (i.e., those at time T) assuming that there are no parameter perturbations,

$$\lambda(\mathbf{x}, T) = 0, \quad \frac{\partial \lambda(\mathbf{x}, T)}{\partial t} = 0, \tag{A-7}$$

and the radiation boundary condition,

$$\lambda(\mathbf{x}, t)|_{\mathbf{x} \rightarrow \infty} \rightarrow 0. \tag{A-8}$$

Using equations A-7 and A-8, equation A-5 can be reduced to:

$$\begin{aligned}
\delta \Delta &= \int_0^T \int_{\Omega} \sum_{r=1}^N \left[d_i^{\text{sim}}(\mathbf{x}, t) * d_{\text{ref}}^{\text{obs}}(\mathbf{x}_f, t) - d_i^{\text{obs}}(\mathbf{x}, t) * d_{\text{ref}}^{\text{sim}}(\mathbf{x}_f, t) \right] d_{\text{ref}}^{\text{obs}}(\mathbf{x}_f, t) \delta(\mathbf{x} - \mathbf{x}_r) \delta d_i^{\text{sim}} dV dt \\
& - \int_0^T \int_{\Omega} \delta c_{ijkl} \frac{\partial d_k^{\text{sim}}}{\partial x_l} \frac{\partial \lambda_i}{\partial x_j} dV dt - \int_0^T \int_{\Omega} \left[\rho \frac{\partial^2 \lambda_i}{\partial t^2} - \frac{\partial}{\partial x_j} \left(c_{ijkl} \frac{\partial \lambda_k}{\partial x_l} \right) \right] \delta d_i^{\text{sim}} dV dt.
\end{aligned} \tag{A-9}$$

According to Plessix (2006), the condition $\frac{\partial \Delta}{\partial \lambda} = 0$ leads to the so-called ‘‘state equations.’’ The adjoint state equations are obtained by setting $\frac{\partial \Delta}{\partial \mathbf{d}^{\text{sim}}} = 0$. Taking the derivative of equation A-9 leads to the adjoint state equation,

$$\begin{aligned}
\rho \frac{\partial^2 \lambda_i}{\partial t^2} - \frac{\partial}{\partial x_j} \left(c_{ijkl} \frac{\partial \lambda_k}{\partial x_l} \right) &= \sum_{r=1}^N \left\{ \left[d_i^{\text{sim}}(\mathbf{x}_r, t) * d_{\text{ref}}^{\text{obs}}(\mathbf{x}_f, t) - d_i^{\text{obs}}(\mathbf{x}_r, t) * d_{\text{ref}}^{\text{sim}}(\mathbf{x}_f, t) \right] d_{\text{ref}}^{\text{obs}}(\mathbf{x}_f, t) \right\} \\
&= \sum_{r=1}^N \left\{ d_{\text{ref}}^{\text{obs}}(\mathbf{x}_f, t) \otimes \left[d_i^{\text{sim}}(\mathbf{x}_r, t) * d_{\text{ref}}^{\text{obs}}(\mathbf{x}_f, t) - d_i^{\text{obs}}(\mathbf{x}_r, t) * d_{\text{ref}}^{\text{sim}}(\mathbf{x}_f, t) \right] \right\},
\end{aligned} \tag{A-10}$$

where \otimes denotes cross-correlation. Because \mathbf{d}^{sim} satisfies the wave equation, Δ is equal to the objective function S_b from equation 2 (see equation A-4) (Plessix, 2006). Hence, the change δS_b caused by the perturbations of the stiffness coefficients is given by:

$$\delta S_b = - \int_0^T \int_{\Omega} \delta c_{ijkl} \frac{\partial d_i^{\text{sim}}}{\partial x_j} \frac{\partial \lambda_k}{\partial x_l} dV dt. \tag{A-11}$$

To simulate the Lagrangian multiplier, we follow Liu and Tromp (2006) in defining the ‘‘adjoint wavefield’’ ψ :

$$\psi(\mathbf{x}, t) \equiv \lambda(\mathbf{x}, T - t). \tag{A-12}$$

The wavefield ψ satisfies the wave equation A-10 but with the source function reversed in time:

$$\rho \frac{\partial^2 \psi_i}{\partial t^2} - \frac{\partial}{\partial x_j} \left(c_{ijkl} \frac{\partial \psi_k}{\partial x_l} \right) = \tag{A-13}$$

$$\sum_{r=1}^N \left\{ d_{\text{ref}}^{\text{obs}}(\mathbf{x}_f, T - t) \otimes \left[d_i^{\text{sim}}(\mathbf{x}_r, T - t) * d_{\text{ref}}^{\text{obs}}(\mathbf{x}_f, T - t) - d_i^{\text{obs}}(\mathbf{x}_r, T - t) * d_{\text{ref}}^{\text{sim}}(\mathbf{x}_f, T - t) \right] \right\}.$$

The initial conditions for ψ are

$$\psi(\mathbf{x}, 0) = 0, \quad \frac{\partial \psi(\mathbf{x}, 0)}{\partial t} = 0, \quad (\text{A-14})$$

and the boundary condition is

$$\psi(\mathbf{x}, t)|_{\mathbf{x} \rightarrow \infty} \rightarrow 0. \quad (\text{A-15})$$

From equations A-10 and A-11, we can find the gradient of the objective function with respect to the stiffness coefficients (Kamath and Tsvankin, 2016):

$$\frac{\partial S}{\partial c_{ijkl}} = - \int_0^T \frac{\partial d_i^{\text{sim}}}{\partial x_j} \frac{\partial \psi_k}{\partial x_l} dt. \quad (\text{A-16})$$

When the model is described by certain parameters m_n instead of c_{ijkl} , the gradient of S can be obtained from the chain rule:

$$\frac{\partial S}{\partial m_n} = \sum_{ijkl} \frac{\partial S}{\partial c_{ijkl}} \frac{\partial c_{ijkl}}{\partial m_n}. \quad (\text{A-17})$$

For VTI media, we define $m_1 = V_{P0}$, $m_2 = V_{S0}$, $m_3 = V_{\text{nmo,P}}$, $m_4 = V_{\text{hor,P}}$, $m_5 = V_{\text{hor,SH}} = V_{S0} \sqrt{1 + 2\gamma}$, and $m_6 = \rho$. The stiffness elements can be expressed using the velocities as follows (e.g., Tsvankin, 2012; Kamath and Tsvankin, 2016):

$$\begin{aligned} C_{11} &= \rho V_{\text{hor,P}}^2, \\ C_{13} &= \rho \left[\sqrt{(V_{P0}^2 - V_{S0}^2)(V_{\text{nmo,P}}^2 - V_{S0}^2)} - V_{S0}^2 \right], \\ C_{33} &= \rho V_{P0}^2, \\ C_{55} &= \rho V_{S0}^2, \\ C_{66} &= \rho V_{\text{hor,SH}}^2. \end{aligned} \quad (\text{A-18})$$

Equations A-17 and A-18 allow us to obtain the derivatives of the objective function with respect to the model parameters:

$$\frac{\partial S}{\partial V_{P0}} = -2\rho V_{P0} \int_0^T \left[\frac{\partial \psi_x}{\partial z} \frac{\partial d_z^{\text{sim}}}{\partial z} + \frac{q}{2} \left(\frac{\partial \psi_x}{\partial z} \frac{\partial d_z^{\text{sim}}}{\partial z} + \frac{\partial \psi_z}{\partial z} \frac{\partial d_x^{\text{sim}}}{\partial x} + \frac{\partial \psi_y}{\partial y} \frac{\partial d_z^{\text{sim}}}{\partial z} + \frac{\partial \psi_z}{\partial z} \frac{\partial d_y^{\text{sim}}}{\partial y} \right) \right] dt, \quad (\text{A-19})$$

$$\begin{aligned} \frac{\partial S}{\partial V_{S0}} &= 2\rho V_{S0} \int_0^T \left[\left(1 + \frac{q}{2} + \frac{1}{2q}\right) \left(\frac{\partial \psi_x}{\partial x} \frac{\partial d_z^{\text{sim}}}{\partial z} + \frac{\partial \psi_z}{\partial z} \frac{\partial d_x^{\text{sim}}}{\partial x} + \frac{\partial \psi_y}{\partial y} \frac{\partial d_z^{\text{sim}}}{\partial z} + \frac{\partial \psi_z}{\partial z} \frac{\partial d_y^{\text{sim}}}{\partial y} \right) \right. \\ &\quad \left. - \left(\frac{\partial \psi_x}{\partial z} + \frac{\partial \psi_z}{\partial x} \right) \left(\frac{\partial d_x^{\text{sim}}}{\partial z} + \frac{\partial d_z^{\text{sim}}}{\partial x} \right) - \left(\frac{\partial \psi_y}{\partial z} + \frac{\partial \psi_z}{\partial y} \right) \left(\frac{\partial d_y^{\text{sim}}}{\partial z} + \frac{\partial d_z^{\text{sim}}}{\partial y} \right) \right] dt, \end{aligned} \quad (\text{A-20})$$

$$\frac{\partial S}{\partial V_{\text{nmo,P}}} = -\frac{\rho V_{\text{nmo,P}}}{q} \int_0^T \left(\frac{\partial \psi_x}{\partial x} \frac{\partial d_z^{\text{sim}}}{\partial z} + \frac{\partial \psi_z}{\partial z} \frac{\partial d_x^{\text{sim}}}{\partial x} + \frac{\partial \psi_y}{\partial y} \frac{\partial d_z^{\text{sim}}}{\partial z} \right) dt, \quad (\text{A-21})$$

$$\frac{\partial S}{\partial V_{\text{hor,P}}} = -2\rho V_{\text{hor,P}} \int_0^T \left(\frac{\partial \psi_y}{\partial y} + \frac{\partial \psi_x}{\partial x} \right) \left(\frac{\partial d_y^{\text{sim}}}{\partial y} + \frac{\partial d_x^{\text{sim}}}{\partial x} \right) dt, \quad (\text{A-22})$$

$$\frac{\partial S}{\partial V_{\text{hor,SH}}} = -2\rho V_{\text{hor,S}} \int_0^T \left[\left(\frac{\partial \psi_x}{\partial y} + \frac{\partial \psi_y}{\partial x} \right) \left(\frac{\partial d_x^{\text{sim}}}{\partial y} + \frac{\partial d_y^{\text{sim}}}{\partial x} \right) - 2 \left(\frac{\partial \psi_y}{\partial y} \frac{\partial d_x^{\text{sim}}}{\partial x} + \frac{\partial \psi_x}{\partial x} \frac{\partial d_y^{\text{sim}}}{\partial y} \right) \right] dt, \quad (\text{A-23})$$

$$\begin{aligned} \frac{\partial S}{\partial \rho} &= - \int_0^T \left\{ V_{P0}^2 \left(\frac{\partial \psi_z}{\partial z} \frac{\partial d_z^{\text{sim}}}{\partial z} \right) + V_{\text{hor,P}}^2 \left(\frac{\partial \psi_x}{\partial x} \frac{\partial d_x^{\text{sim}}}{\partial x} + \frac{\partial \psi_y}{\partial y} \frac{\partial d_y^{\text{sim}}}{\partial y} + \frac{\partial \psi_x}{\partial x} \frac{\partial d_y^{\text{sim}}}{\partial y} + \frac{\partial \psi_y}{\partial y} \frac{\partial d_x^{\text{sim}}}{\partial x} \right) \right. \\ &\quad + V_{S0}^2 \left[\left(\frac{\partial \psi_x}{\partial z} + \frac{\partial \psi_z}{\partial x} \right) \left(\frac{\partial d_x^{\text{sim}}}{\partial z} + \frac{\partial d_z^{\text{sim}}}{\partial x} \right) + \left(\frac{\partial \psi_y}{\partial z} + \frac{\partial \psi_z}{\partial y} \right) \left(\frac{\partial d_y^{\text{sim}}}{\partial z} + \frac{\partial d_z^{\text{sim}}}{\partial y} \right) \right] \\ &\quad + V_{\text{hor,SH}}^2 \left[\left(\frac{\partial \psi_x}{\partial y} + \frac{\partial \psi_y}{\partial x} \right) \left(\frac{\partial d_x^{\text{sim}}}{\partial y} + \frac{\partial d_y^{\text{sim}}}{\partial x} \right) - 2 \frac{\partial \psi_y}{\partial y} \frac{\partial d_x^{\text{sim}}}{\partial x} - 2 \frac{\partial \psi_x}{\partial x} \frac{\partial d_y^{\text{sim}}}{\partial y} \right] \\ &\quad \left. + \left[\sqrt{(V_{\text{nmo,P}}^2 - V_{S0}^2)(V_{P0}^2 - V_{S0}^2)} - V_{S0}^2 \right] \left[\frac{\partial \psi_z}{\partial z} \frac{\partial d_x^{\text{sim}}}{\partial x} + \frac{\partial \psi_x}{\partial x} \frac{\partial d_z^{\text{sim}}}{\partial z} + \frac{\partial \psi_z}{\partial z} \frac{\partial d_y^{\text{sim}}}{\partial y} + \frac{\partial \psi_y}{\partial y} \frac{\partial d_z^{\text{sim}}}{\partial z} \right] \right. \\ &\quad \left. + v_x \psi_x + v_y \psi_y + v_z \psi_z \right\} dt, \end{aligned} \quad (\text{A-24})$$

where

$$q = \sqrt{\frac{V_{\text{nmo,P}}^2 - V_{\text{S0}}^2}{V_{\text{P0}}^2 - V_{\text{S0}}^2}}. \quad (\text{A-25})$$

Here, \mathbf{v} and ψ are the forward- and back-propagated velocity fields, respectively.

REFERENCES

- Alkhalifah, T., and R. É. Plessix, 2014, A recipe for practical full-waveform inversion in anisotropic media: An analytical parameter resolution study: *Geophysics*, **79**, R91–R101.
- Asnaashari, A., R. Brossier, S. Garambois, F. Audebert, P. Thore, and J. Virieux, 2012, Time-lapse imaging using regularized FWI: a robustness study: *SEG Technical Program Expanded Abstracts*, 1–5.
- , 2015, Time-lapse seismic imaging using regularized full-waveform inversion with a prior model: Which strategy?: *Geophysical Prospecting*, **63**, 78–98.
- Bai, T., and I. Tsvankin, 2019, Source-independent waveform inversion for attenuation estimation in anisotropic media: *Geophysical Prospecting*, **67**, 2343–2357.
- Choi, Y., and T. Alkhalifah, 2011, Source-independent time-domain waveform inversion using convolved wavefields: Application to the encoded multisource waveform inversion: *Geophysics*, **76**, R125–R134.
- Choi, Y., and D.-J. Min, 2012, Source-independent elastic waveform inversion using a logarithmic wavefield: *Journal of Applied Geophysics*, **76**, 13–22.
- Choi, Y., C. Shin, D. J. Min, and T. Ha, 2005, Efficient calculation of the steepest descent direction for source-independent seismic waveform inversion: An amplitude approach: *Journal of Computational Physics*, **208**, 455–468.
- Denli, H., and L. Huang, 2009, Double-difference elastic waveform tomography in the time domain: *SEG Technical Program Expanded Abstracts*, 2302–2306.
- Hale, D., 2013, Dynamic warping of seismic images: *Geophysics*, **78**, S105–S115.
- Holschuh, N. D., C. Li, M. A. Meadows, and S. Dobbs, 2014, Systems and methods for aligning a monitor seismic survey with a baseline seismic survey. (U. S. Patent 14,565,117: Chevron USA Inc., 1–16).
- Kamath, N., and I. Tsvankin, 2013, Full-waveform inversion of multicomponent data for horizontally layered VTI media: *Geophysics*, **78**, WC113–WC121.
- , 2016, Elastic full-waveform inversion for VTI media: Methodology and sensitivity analysis: *Geophysics*, **81**, C53–C68.
- Lee, K. H., and H. J. Kim, 2003, Source-independent full-waveform inversion of seismic data: *Geophysics*, **68**, 2010–2015.
- Li, C., M. Meadows, and T. Dygert, 2019, Warping least-squares inversion for 4d velocity change: Gulf of Mexico case study: *Interpretation*, **7**, SB23–SB31.
- Liu, Q., and J. Tromp, 2006, Finite-frequency kernels based on adjoint methods: *Bulletin of the Seismological Society of America*, **96**, 2383–2397.
- Liu, Y., and I. Tsvankin, (accepted) 2021, Methodology of time-lapse elastic full-waveform inversion for VTI media: *Journal of Seismic Exploration*.
- Lumley, D., 2010, 4D seismic monitoring of CO₂ sequestration: *Leading Edge*, 150–155.
- Luo, C. M., S. X. Wang, and S. Y. Yuan, 2014, Effect of inaccurate wavelet phase on prestack waveform inversion: *Journal of Applied Geophysics*, **11**, 479–488.
- Pevzner, R., M. Urosevic, D. Popik, V. Shulakova, K. Tertyshnikov, E. Caspari, J. Correa, T. Dance, A. Kepic, S. Glubokovskikh, S. Ziramov, B. Gurevich, R. Singh, M. Raab, M. Watson, T. Daley, M. Robertson, and B. Freifeld, 2017, 4D surface seismic tracks small supercritical CO₂ injection into the subsurface: CO₂CRC Otway Project: *International Journal of Greenhouse Gas Control*, **63**, 150–157.
- Plessix, R. E., 2006, A review of the adjoint-state method for computing the gradient of a functional with geophysical applications: *Geophysical Journal International*, **167**, 495–503.
- Plessix, R.-E., S. Michelet, H. Rynja, H. Kuehl, C. Perkins, J. Maag, and P. Hatchell, 2010, Some 3D applications of full waveform inversion: *EAGE Expanded Abstracts*.
- Pratt, R. G., 1999, Seismic waveform inversion in the frequency domain, part 1: Theory and verification in a physical scale model: *Geophysics*, **64**, 888–901.
- Rickett, J., L. Duranti, T. Hudson, B. Regel, and N. Hodgson, 2007, 4d time strain and the seismic signature of geomechanical compaction at genesis: *The Leading Edge*, **26**, 644–647.

- Seo, T., C. Shin, and D. Min, 2005, Efficient calculation of steepest descent direction of source signature independent waveform inversion of logarithmic wavefield: SEG Technical Program Expanded Abstracts, 1838–1841.
- Singh, S., I. Tsvankin, and E. Zahibi Naeini, 2018, Bayesian framework for elastic full-waveform inversion with facies information: *Leading Edge*, **37**, 924–931.
- , 2019, Bayesian approach to facies-constrained waveform inversion for VTI media: SEG Technical Program Expanded Abstracts, 1370–1374.
- Smith, S. S., and I. Tsvankin, 2013, Sensitivity of compaction-induced multicomponent seismic time shifts to variations in reservoir properties: *Geophysics*, **78**, T151–T163.
- Song, Z., P. R. Williamson, and R. G. Pratt, 1995, Frequency-domain acoustic-wave modeling and inversion of crosshole data: Part ii—inversion method, synthetic experiments and real-data results: *Geophysics*, **60**, 796–809.
- Tarantola, A., 1984, Linearized inversion of seismic reflection data: *Geophysical Prospecting*, **32**, 998–1015.
- Tsvankin, I., 2012, *Seismic signatures and analysis of reflection data in anisotropic media*, third edition: Society of Exploration Geophysicists.
- Venstad, J. M., 2014, Dynamic time warping — an improved method for 4d and tomography time shift estimation?: *Geophysics*, **79**, R209–R220.
- Vigh, D., K. Jiao, D. Watts, and D. Sun, 2014, Elastic full-waveform inversion application using multicomponent measurements of seismic data collection: *Geophysics*, **79**, R63–R77.
- Warner, M., A. Ratcliffe, T. Nangoo, J. Morgan, A. Umpleby, N. Shah, V. Vinje, I. Štekl, L. Guasch, C. Win, G. Conroy, and A. Bertrand, 2013, Anisotropic 3d full-waveform inversion: *Geophysics*, **78**, R59–R80.
- Watanabe, T., S. Shimizu, E. Asakawa, and T. Matsuoka, 2004, Differential waveform tomography for time-lapse crosswell seismic data with application to gas hydrate production monitoring: SEG Technical Program Expanded Abstracts, 2323–2326.
- Xu, K., S. A. Greenhalgh, and M. Wang, 2006, Comparison of source-independent methods of elastic waveform inversion: *Geophysics*, **71**, R91–R100.
- Yuan, F., S. Wang, S. Yuan, J. Wang, J. Li, P. Shi, and Y. Liu, 2014, Influence of inaccurate wavelet amplitude on frequency-domain full waveform inversion: EAGE Conference Expanded Abstracts, 1–5.
- Zhang, Q., H. Zhou, Q. Li, H. Chen, and J. Wang, 2016, Robust source-independent elastic full-waveform inversion in the time domain: *Geophysics*, **81**, R29–R44.
- Zhou, B., and S. A. Greenhalgh, 2003, Crosshole seismic inversion with normalized full-waveform amplitude data: *Geophysics*, **68**, 1320–1330.